

# Weak localization in graphene flakes

F. V. Tikhonenko, D. W. Horsell, R. V. Gorbachev, and A. K. Savchenko

*School of Physics, University of Exeter,*

*Stocker Road, Exeter, EX4 4QL, U.K.*

## Abstract

We show that the manifestation of quantum interference in graphene is very different from that in conventional two-dimensional systems. Due to the chiral nature of charge carriers, it is sensitive not only to inelastic, phase-breaking scattering, but also to a number of elastic scattering processes. We study weak localization in different samples and at different carrier densities, including the Dirac region, and find the characteristic rates that determine it. We show how the shape and quality of graphene flakes affect the values of the elastic and inelastic rates and discuss their physical origin.

PACS numbers: 73.23.-b, 72.15.Rn, 73.43.Qt

The quantum correction to the conductivity of two-dimensional systems due to electron interference has been studied for more than twenty years [1, 2]. This phenomenon of weak localization (WL) has become a tool to determine the processes responsible for electron dephasing due to inelastic electron scattering or scattering by magnetic impurities [2, 3]. In this well-established field of research it comes as a surprise to discover that in a new two-dimensional system, graphene [4], WL does not follow the standard convention that it is only controlled by inelastic and spin-flip processes. First attempts to measure WL in graphene have produced contradictory results that tentatively point towards this unusual behavior [5, 6, 7]. Measurements on graphene flakes fabricated by mechanical exfoliation [5] have shown that in the majority of samples WL is totally suppressed. In contrast, in a sample fabricated by an alternative, epitaxial method, WL has been distinctly seen, albeit at a single (high) carrier density [7].

The theory of WL in graphene [8] predicts a remarkable feature: it should be sensitive not only to inelastic, phase breaking processes, but also to different *elastic* scattering mechanisms [8, 9, 10]. The reason for this is that charge carriers in graphene are *chiral*, that is, they have an additional quantum number (pseudospin) [11]. Elastic scattering that breaks the chirality will destroy the interference within each of the two graphene valleys in  $k$ -space. Such defects, characterised by the scattering rate  $\tau_s^{-1}$ , include surface ripples, dislocations and atomically sharp defects [5, 10]. Intra-valley WL can also be destroyed by anisotropy of the Fermi surface in  $k$ -space, so called ‘trigonal warping’ [8], characterised by the rate  $\tau_w^{-1}$ . There is one elastic process, however, which acts to restore the suppressed interference. This is *inter*-valley scattering, which occurs at a rate  $\tau_i^{-1}$  on defects with size of the order of the lattice spacing  $a$ . As the two valleys have opposite chirality and warping, inter-valley scattering is expected to negate the chirality breaking and warping effects by allowing interference of carriers from different valleys.

In this work we aim to examine what factors are responsible for the manifestation of WL in graphene fabricated by mechanical exfoliation [4]. We study the magnetoconductivity (MC) in perpendicular field of several samples with different quality and dimensions, with the aim to control the relation between the scattering rates of carriers. These studies are performed at different carrier densities controlled by a gate voltage  $V_g$ , which include densities around the Dirac point at  $V_g = 0$ . This point is special as about it there is a change of the type of carrier from electrons to holes and therefore the net carrier density is zero. The conductivity,

however, is seen to remain at a finite value  $\sigma_{\min} \sim e^2/h$  and not drop to zero [12].

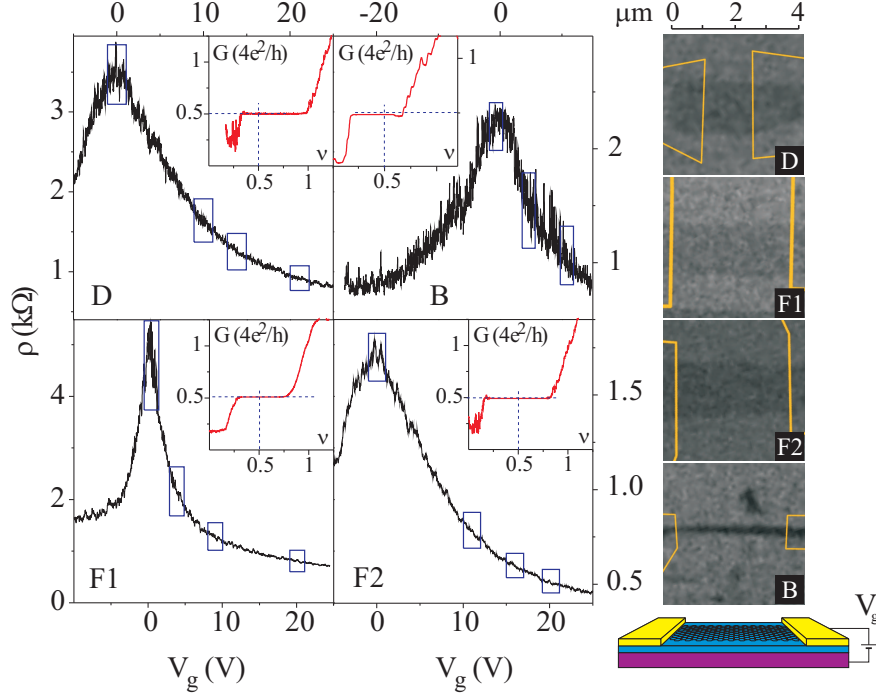


FIG. 1: Resistivity of graphene flakes as a function of  $V_g$  at  $T = 0.25$  K. The mobilities (in  $\text{cm}^2\text{V}^{-1}\text{s}^{-1}$ ) of the samples outside the Dirac region: 5100 (D), 7500 (F1), 10000 (F2) and 8000 (B). The insets show the first quantum Hall plateau, where filling factor  $\nu = nh/4eB$ . The right panel shows SEM images of the samples, where the positions of the contacts are shown as outlines. The diagram at the foot of this panel shows the graphene sample on  $n^+$ Si substrate (purple), covered by 300 nm  $\text{SiO}_2$  (blue) and contacted by Au/Cr (yellow). Control of the carrier density  $n$  is achieved by  $V_g$ .

Figure 1 shows the resistivity as a function of  $V_g$  of four samples with different shapes and mobilities: D, F1, F2 and B, each with a typical peak around the Dirac point. Sample D is a square flake; F1 and F2 are rectangular with similar width to, but length larger than D; B is a narrow strip of similar length to F1 and F2 but with much smaller width, Fig. 1 (right). Insets in Fig. 1 demonstrate measurements of the first quantum Hall plateau, which shows a half-integer step ( $0.5 \times 4e^2/h$ ) – a clear indication that the samples are single-layer graphene [12]. We wanted to see what difference the shape of the samples will make to the WL – e.g., the narrowest sample B is expected to have the largest scattering rate  $\tau_i^{-1}$ , as the edges could produce strong inter-valley scattering. To understand the relation between the

scattering and the details of the graphene surface, the electrical measurements have been complemented by atomic force microscope (AFM) imaging of the sample topography, which have shown the presence of ripples, and additional rapid folds (ridges) across sample B (see Supplementary Material below).

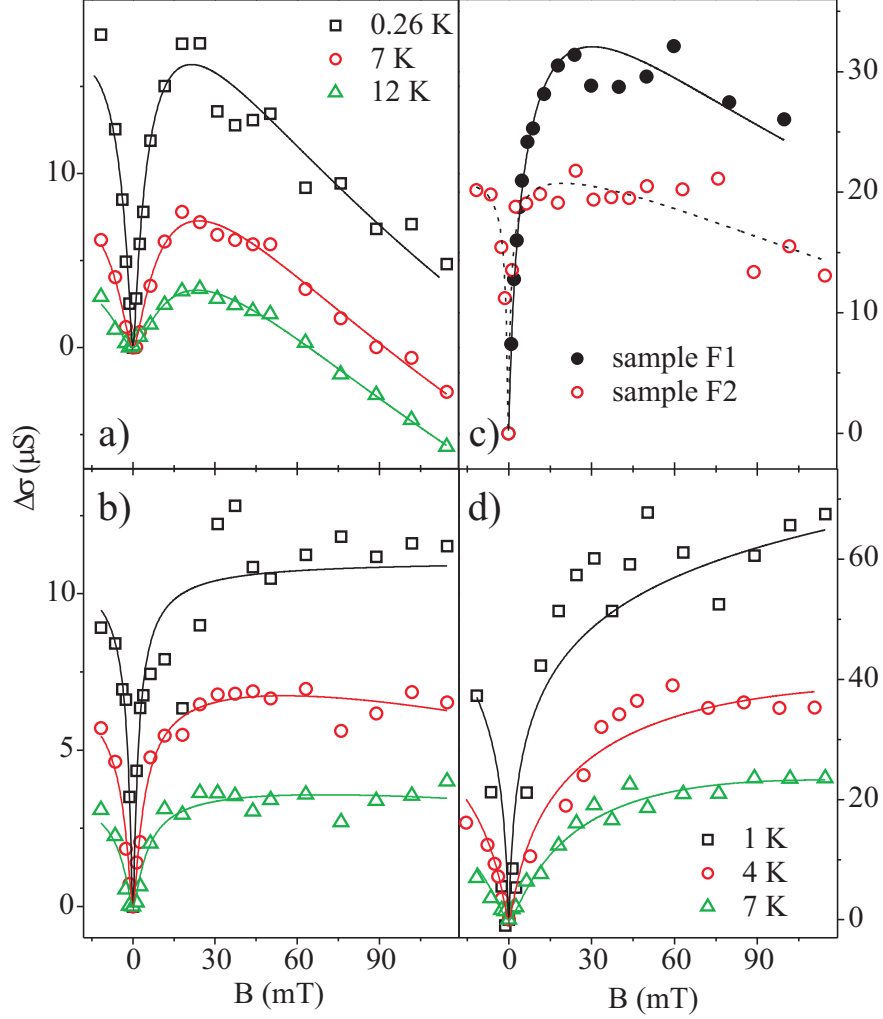


FIG. 2: (color online) Magnetoconductivity observed in graphene flakes. (a) Dirac region of sample D,  $|V_g| \lesssim 1$  V,  $n \lesssim 7 \times 10^{10} \text{ cm}^{-2}$ ; (b) sample D,  $V_g \simeq 14$  V,  $n \simeq 10^{12} \text{ cm}^{-2}$  (the legends of (a) and (b) are the same); (c) samples F1 and F2 at  $T = 1$  K,  $V_g \simeq 10$  V,  $n \simeq 7 \times 10^{11} \text{ cm}^{-2}$ ; (d) sample B,  $V_g \simeq 11$  V,  $n \simeq 8 \times 10^{11} \text{ cm}^{-2}$ . Lines are best fits to Eq. 1.

In order to study the conductivity correction caused by WL we must first account for the reproducible conductance fluctuations clearly seen in Fig. 1. They are also present as a function of magnetic field  $B$  and are caused by the fact that the graphene flakes are small (comparable to the dephasing length  $L_\phi$ ), so that the average effect of WL is of the same

order as the fluctuations which have the same, quantum interference origin [2]. We use the procedure developed in [13] in the study of WL in bilayer graphene:  $R(V_g)$  is measured at different  $B$  and the results are averaged over a range  $\Delta V_g = 2\text{ V}$  shown in Fig. 1 by boxes which contain a large number of fluctuations (see Supplementary Material below). Examples of the obtained average MC,  $\Delta\sigma(B) = \langle\sigma(V_g, B) - \sigma(V_g, 0)\rangle_{\Delta V_g}$ , are shown in Fig. 2 for different samples. For the analysis of the results we use the theory [8] which predicts that the MC is controlled by several scattering rates, both inelastic ( $\tau_\phi^{-1}$ ) and elastic ( $\tau_i^{-1}$ ,  $\tau_s^{-1}$ ,  $\tau_w^{-1}$ ):

$$\begin{aligned} \frac{\pi h}{e^2} \cdot \Delta\sigma(B) = & F\left(\frac{\tau_B^{-1}}{\tau_\phi^{-1}}\right) - F\left(\frac{\tau_B^{-1}}{\tau_\phi^{-1} + 2\tau_i^{-1}}\right) \\ & - 2F\left(\frac{\tau_B^{-1}}{\tau_\phi^{-1} + \tau_i^{-1} + \tau_w^{-1}}\right). \end{aligned} \quad (1)$$

Here  $F(z) = \ln z + \psi(0.5 + z^{-1})$ ,  $\psi(x)$  is the digamma function,  $\tau_B^{-1} = 4eDB/\hbar$ ,  $\tau_\phi^{-1}$  is the phase-breaking rate and  $\tau_*^{-1} = \tau_s^{-1} + \tau_w^{-1}$ . (The theory assumes that the momentum relaxation rate  $\tau_p^{-1}$  is the highest in the system and comes from the Coulomb charges in the SiO<sub>2</sub> substrate and not atomically sharp defects, so that it does not affect the carrier chirality.) The first term in Eq. (1) is responsible for weak localization, while the terms with negative sign can result in 'anti-localization'.

We have found that among the different possible relations between the scattering rates, the following holds in all studied samples: the intra-valley WL is strongly suppressed due to a large rate  $\tau_*^{-1}$ , which approaches  $\tau_p^{-1}$ ; however, WL is clearly seen in all regions of the carrier density, due to significant intra-valley scattering,  $\tau_i^{-1} \sim \tau_\phi^{-1}$ . At the same time, the shape of the MC curves can be very different as it is controlled by the interplay between all scattering rates involved, Fig. 2. Comparing two regions of carrier densities for square sample D (Dirac region (a) and electron region (b)) one can see that in (a) the curves have a much stronger downturn, indicating greater importance of the third ('anti-localising') term in Eq. 1 due to smaller rate  $\tau_*^{-1}$ . For two geometrically similar samples F1 and F2 in Fig. 2(c), it is seen that sample F2 (with largest mobility) has a more rapid increase of the conductivity in smaller field (due to smaller  $\tau_\phi^{-1}$ ) and more rapid downward turn of the curves at larger fields (due to smaller  $\tau_i^{-1}$ ). For the narrow sample B, Fig. 2(d), the MC curves do not turn down at all, indicating a very fast inter-valley rate  $\tau_i^{-1}$  and therefore unimportance of all terms in Eq. 1 apart from the first.

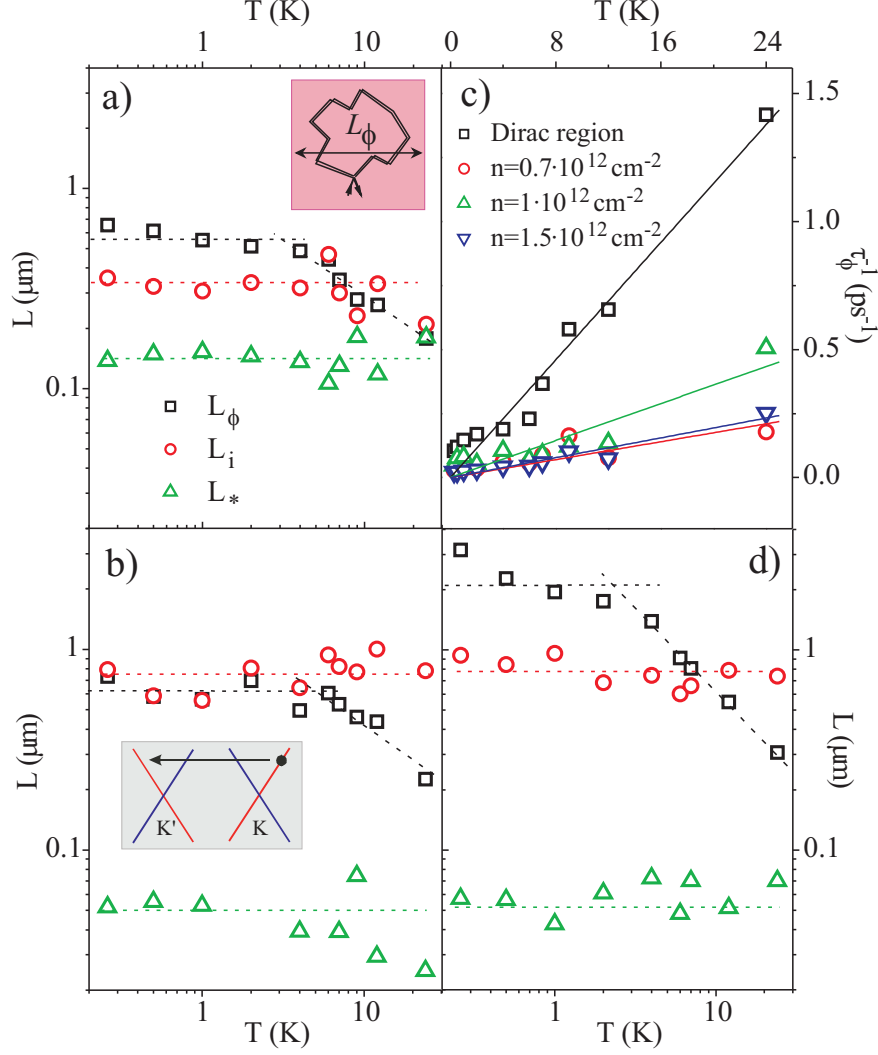


FIG. 3: (color online) Characteristic lengths responsible for weak localization; dotted lines are guides to the eye. Sample D: (a) the Dirac region ( $n \lesssim 7 \times 10^{10} \text{ cm}^{-2}$ ) and (b) electron region ( $n \simeq 10^{12} \text{ cm}^{-2}$ ); (c) Phase-breaking rate  $\tau_\phi^{-1} = D/L_\phi^2$  as a function of  $T$  for different  $n$ . Inset to (a) illustrates the saturation of  $L_\phi$  at low  $T$  due to the sample size. Inset to (b) shows the scattering process behind the length  $L_i$ . Sample F2: (d) Temperature dependence of the characteristic lengths in the electron region ( $n \simeq 10^{12} \text{ cm}^{-2}$ ).

Figure 3 shows the temperature dependence of the characteristic lengths found from the analysis of the MC by the best fit with Eq. 1. Figure 3(a,b) compares the results for the Dirac and electron regions for sample D, where it is seen that  $L_\phi$  is temperature dependent at high  $T$  ( $\geq 3 \text{ K}$ ) but saturates at a value  $L_\phi^{\text{sat}}$  at low temperatures. Figure 3(b,d) compares the results for samples D and F2, at close values of carrier densities outside the Dirac region.

Sample F2 is about three times longer, and one can see that  $L_\phi^{\text{sat}}$  is larger in the longer sample F2. (In sample B,  $L_\phi^{\text{sat}}$  has also been found to be larger than in sample D.) This clearly implies that the reason for the saturation is a limitation imposed by the sample size, and not by scattering from a small, uncontrolled number of magnetic impurities [3].

In the Dirac region  $L_\phi^{\text{sat}}$  has been found to have a smaller value than at larger carrier densities. (It is interesting to note that the narrow sample, B, shows the biggest decrease of  $L_\phi^{\text{sat}}$  in the Dirac region, while the square sample, D, the smallest.) This decrease can be related to the inhomogeneity of the sample at low carrier densities. It can result in formation of electron-hole puddles, so that at  $V_g = 0$  there are equal densities of electrons and holes and not zero density of each type of carrier. Inhomogeneity can modify the geometry of conducting paths and decrease the effective dimensions of the sample, resulting in a smaller value of  $L_\phi^{\text{sat}}$ .

The temperature dependence of  $L_\phi$  contains information about the inelastic mechanism responsible for the dephasing of charge carriers. There are suggestions that electron-electron ( $e$ - $e$ ) interaction, the main mechanism of dephasing at low  $T$ , is different in graphene compared with other systems [14]. To examine this we have analyzed the  $T$ -dependence of the dephasing rates found from analysis of the WL. Figure 3(c) shows the phase-breaking rate in different density regions of sample D. (To find  $\tau_\phi^{-1}$  we use the relation  $L_\phi = (D\tau_\phi)^{1/2}$ , where the diffusion coefficient  $D = v_F l/2$  is determined from the mean free path  $l = \hbar/2e^2 k_F \rho$ . For the Dirac region, where the puddles can be formed, the value of the Fermi wavenumber  $k_F$  (inside the puddle) is simply estimated at the boundary of the region where the MC is studied,  $|V_g| = 1$  V, Fig. 1.) Our results show that electron dephasing rate obeys the usual, linear  $T$ -dependence for  $e$ - $e$  scattering in the ‘dirty limit’,  $T\tau_p < 1$  [1]:  $\tau_\phi^{-1} = \beta k_B T \ln g / \hbar g$ , where  $g = \sigma \hbar / e^2$ . (In our samples the parameter  $T\tau_p$  varies from 0.002 to 0.4 in the studied temperature range 0.25–25 K.) The empirical coefficient  $\beta$  is found to be between 1 and 2 in all studied regions, Fig. 3(c), and all samples. Therefore, we can conclude that while electron interference in graphene is significantly different from other systems,  $e$ - $e$  interaction does not show unconventional behavior.

In addition to the analysis of the WL, we have also analyzed conductance fluctuations as a function of  $B$  and  $V_g$  using standard relations in terms of  $L_\phi$  [2]. This analysis has given values of  $L_\phi$  close to those found from the analysis of WL (see Supplementary Material below).

Now let us discuss the behavior of the elastic, inter-valley length  $L_i$  which we have verified to be essentially  $T$ -independent in all samples. In samples D, F1 and F2 the found  $L_i$  is comparable to the width of the samples (approximately half the width). This means that, indeed, the sample edges make significant contributions to inter-valley scattering. This is consistent with the fact that the narrowest sample B has shown the smallest value of  $L_i$ . However, the value of  $L_i$  for sample B is about three times smaller than the sample width. This can be due to the presence of rapid ridges of height  $\sim 1.5$  nm observed in this sample by AFM, Fig. 4(a). They are separated by a distance smaller than the sample width and can be another source of inter-valley scattering. This suggests that the inter-valley scattering is controlled not only by the edges but also by the defects in the inner part of the sample.

We have found that the intra-valley scattering length  $L_*$  is much smaller than the inter-valley length  $L_i$ , Fig. 3, and approaches the mean free path. There are several possible mechanisms that can be responsible for the observed large intra-valley scattering rate and resulting strong suppression of WL in one valley (see Supplementary Material below). Scattering by *atomically-sharp defects* cannot explain this: such scattering is also a source of strong inter-valley scattering, so that  $L_i$  and  $L_*$  would be comparable if this mechanism was dominant. The smaller value of  $L_*$  in experiment must therefore be due to an additional scattering rate which affects  $L_*$  but not  $L_i$ : from *warping* [8], or from the defects of the crystal structure that are large on the atomic scale [5, 10]. Estimation of the expected  $\tau_w^{-1}$  using theory [8] gives a value of  $\tau_w^{-1} \leq 0.3$  ps $^{-1}$  which is much smaller than the experimental  $\tau_s^{-1} \sim 10$  ps $^{-1}$ . Therefore, the reason for small  $L_*$  could lie in the defects of the crystal structure of graphene flakes: *ripples* and *dislocations*. (The strain in the lattice induced by such defects acts as a source of effective magnetic field that can destroy WL.) As the dislocation core is also a source of inter-valley scattering, their separation can be estimated from the known value of  $L_i$ . This value is much larger than the dislocation separation  $\xi \sim 50$  nm required to explain the small value of  $L_*$ . (This value of  $\xi$  is obtained using the relation  $\tau_s^{-1} = v_F/k_F \xi^2$  [10].) The effect of ripples on the graphene surface is also negligible in our samples, if we use the estimation of this effect from [5]. The roughness of our samples found from AFM measurements, Fig. 4(b,c), is  $h \simeq 0.3$  nm and  $d \simeq 10$  nm (in agreement with [15]), which gives for a typical  $L_\phi \approx 1$   $\mu$ m an effective magnetic field  $B_{\text{eff}} \sim 1$  mT. This is a small correction to the real fields used in experiment, Fig. 2. There is one more mechanism that can introduce an asymmetry in the crystal structure and hence break the



chirality of carriers: a potential gradient coming from charged impurities in the substrate. Our estimation of its effect using the approach of [10] has also given a negligible result (see Supplementary Material below). Therefore, the obtained values of the scattering rate  $\tau_*^{-1}$  are much higher than those predicted by existing models, and more detailed theories of the mechanisms of intra-valley suppression of WL in graphene are required.

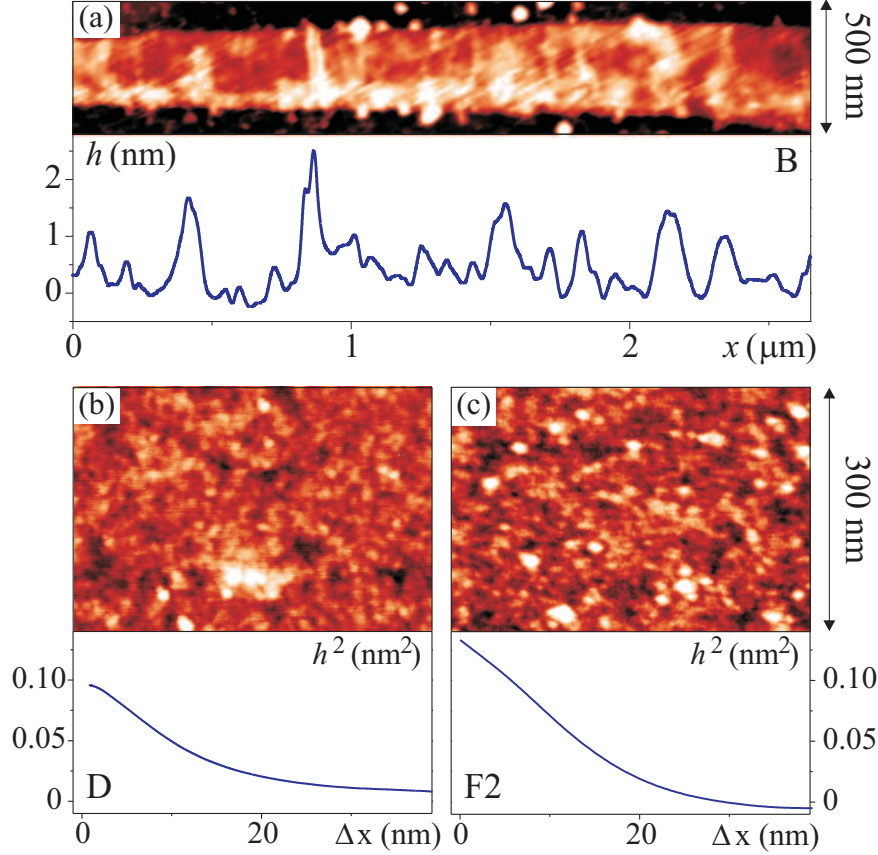


FIG. 4: Atomic force microscope images of graphene surfaces. Below the image of sample B (a) is the surface profile averaged over the width of the sample. Below the images of the topography of samples D (b) and F2 (c) are the corresponding autocorrelation functions of the surface roughness.

In summary, we have shown that the weak localization correction in graphene exists at all studied carrier densities, including the Dirac region. Its manifestation is determined by the interplay of inelastic and elastic scattering mechanisms, which makes WL a sensitive tool to detect the defects responsible for inter-valley scattering and chirality breaking. We show that, in spite of a strong intra-valley suppression of WL, the quantum interference correction to the conductivity is clearly seen due to significant inter-valley scattering. Total suppression of WL is only possible in experiments where inter-valley scattering is negligible,

i.e. in very large samples without sharp defects in the bulk.

We gratefully acknowledge stimulating discussions with E. McCann, V. V. Cheianov, F. Guinea and V. I. Fal'ko, and thank B. Wilkinson for assistance at an early stage of the experiments.

- 
- [1] B. L. Altshuler, D. Khmelnitzkii, A. I. Larkin, and P. A. Lee, Phys. Rev. B **22**, 5142 (1980); G. Bergman, Phys. Rep. **107**, 1 (1984).
  - [2] C. W. J. Beenakker, and H. Van Houten, Solid State Physics **44**, 1 (edt. by H. Ehrenreich and D. Turnbull, Academic Press Inc., San Diego, 1991).
  - [3] F. Pierre, A. B. Gougam, A. Anthore, H. Pothier, D. Esteve, and N. O. Birge, Phys. Rev. B **68** 085413 (2003).
  - [4] K. S. Novoselov, *et al.*, Science **306**, 666 (2004).
  - [5] S. V. Morozov, *et al.*, Phys. Rev. Lett. **97**, 016801 (2006).
  - [6] H. B. Heersche *et al.*, Nature **446**, 56 (2007).
  - [7] X. Wu, X. Li, Z. Song, C. Berger, and W. A. de Heer, Phys. Rev. Lett. **98**, 136801 (2007).
  - [8] E. McCann, *et al.*, Phys. Rev. Lett. **97**, 146805 (2006).
  - [9] H. Suzuura, and T. Ando, Phys. Rev. Lett. **89**, 266603 (2002).
  - [10] A. F. Morpurgo, and F. Guinea, Phys. Rev. Lett. **97**, 196804 (2006).
  - [11] T. Ando, T. Nakanishi, and R. Saito, J. Phys. Soc. Japan **67**, 2857 (1998).
  - [12] A. K. Geim, and K. S. Novoselov, Nature Mat. **6**, 183 (2007).
  - [13] R. V. Gorbachev, F. V. Tikhonenko, A. S. Mayorov, D. W. Horsell and A. K. Savchenko, Phys. Rev. Lett. **98**, 176805 (2007).
  - [14] J. Gonzalez, F. Guinea, and M. A. H. Vozmediano, Phys. Rev. Lett. **77**, 3589 (1996); J. Gonzalez, F. Guinea, and M. A. H. Vozmediano, Phys. Rev. B **59**, R2474 (1999); S. Das Sarma, E. H. Hwang and W-K. Tse, Phys. Rev. B **75**, 121406(R) (2007); M. Polini, R. Asgari, Y. Barlas, T. Pereg-Barnea and A. H. MacDonald, arXiv:0704.3786.
  - [15] M. Ishigami, J. H. Chen, W. G. Cullen, M. S. Fuhrer, and E. D. Williams, Nano Letters **7**, 1643 (2007).

# Weak localisation in graphene flakes: Supplementary material

F. V. Tikhonenko, D. W. Horsell, R. V. Gorbachev, and A. K. Savchenko

*School of Physics, University of Exeter, Stocker Road, Exeter, EX4 4QL, U.K.*

## Samples

Samples were manufactured using the method of mechanical exfoliation of highly-oriented pyrolytic graphite devised in [4], on a  $n^+\text{Si}/\text{SiO}_2$  substrate with oxide layer of thickness  $t = 300$  nm. Lithographically defined Au/Cr contacts were subsequently made to each flake. Resistance measurements were carried out in the temperature range from 0.25 to 25 K using a standard lock-in technique with 1 nA driving current. Samples B, D, F1 are two-terminal and F2 is four-terminal (the additional contacts were used to account for the contact resistance). The concentration of carriers (electrons  $n$  and holes  $p$ ) in graphene is determined by the capacitance between the graphene and  $n^+\text{Si}$  substrate:  $e(p - n) = (\epsilon\epsilon_0/t)V_g$ . There was a small unintentional doping of the samples leading to a shift in gate voltage ( $\sim 5$  V) of the position of the resistance peak with respect to  $V_g = 0$ , which has been accounted for in the main text. The graphene–Au/Cr contact resistance has been found from the deviation of the height of the quantum Hall plateau from the expected value of  $2e^2/h$  (see insets to Fig. 1 of main text). The values of the contact resistance for samples F1 and D are about  $\sim 100\ \Omega$  and  $\sim 600\ \Omega$  for sample B.

## Averaging procedure and analysis of magnetoconductance

A method of effective averaging is important in small-sized samples to remove the influence of mesoscopic fluctuations, as without it one can get contradictory results for the magnetoconductance (MC). (If we attempt to measure  $\Delta\sigma(B)$  at different  $V_g$ , the character of the MC depends on the specific point in  $V_g$  at which it is measured). Figure 1 shows how the averaging is performed. For each temperature the conductivity of the sample as a function of the gate voltage is first measured across a 2 V range at incremental values of the magnetic field. Then the curve at zero magnetic field is subtracted from each curve and the resulting difference is averaged across the 2 V gate voltage range. One can see from Fig. 1

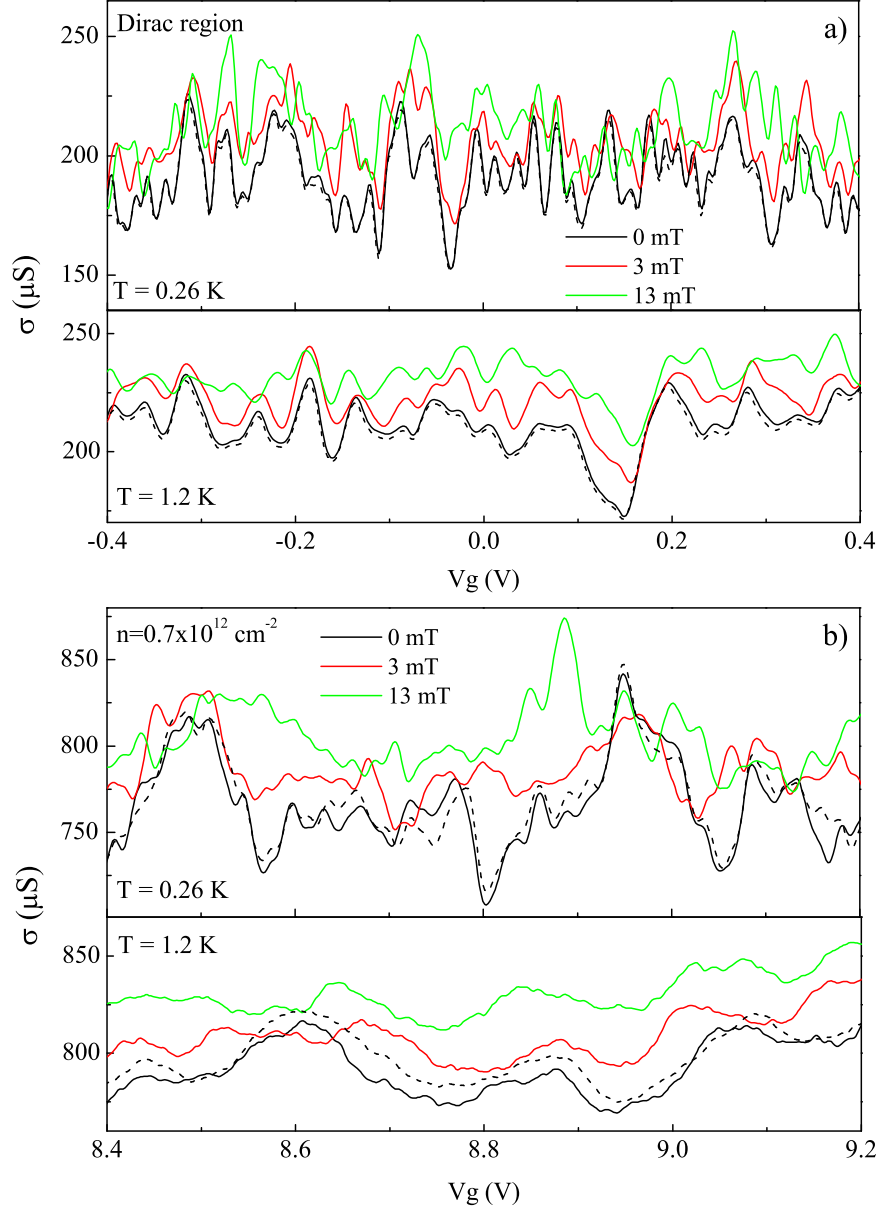


FIG. 1: Illustration of the averaging procedure of the magnetoconductance of sample F1 in two density regions at two temperatures (only a fraction of  $\Delta V_g$  is shown here): (a) Dirac region, (b) electron region. Dotted lines show repeated sweeps at  $B = 0$ .

the average increase of  $\langle \Delta \sigma \rangle_{\Delta V_g}$  with magnetic field. These averaged values of the MC are plotted as a function of  $B$  in Figure 2 of the main text.

The perturbation theory of weak localization (WL) is applicable at  $k_F l \gg 1$  (a diffusive metal). In our samples  $k_F l$ , found from the conductivity  $\sigma = 2e^2(k_F l)/h$ , varies in the range 3–30, with the smallest values in the Dirac region: 4, 3, 8 and 6 for samples D, F1, F2 and B,

respectively. Another limitation for the application of the diffusive theory of WL is  $B \lesssim B_{\text{tr}}$ , where the ‘transport’ magnetic field is found from the condition  $L_B = (\hbar/eB)^{1/2} \approx l$ . This limits the range of magnetic fields where we perform the analysis to  $B \leq 100$  mT.

For the narrowest sample B, the dephasing length is larger than its width and therefore the 1D theory of WL [8] should be used in the analysis of its MC in small fields. However, at fields where  $L_B < W$  ( $W$  is the width of the sample) i.e. at  $B > 7$  mT, the 2D theory becomes applicable. As the bulk of the data is obtained in this range of the field, we have used 2D theory (Eq. 1 in main text) to analyse the MC.

### Comparison of characteristic lengths and times

Figure 2 shows for samples F1, F2 and D a comparison of the length  $L_*$  with length  $L_i$ , as well as the values of the corresponding times  $\tau_*$  and  $\tau_i$  (using  $L_x = (D\tau_x)^{1/2}$ ) for different carrier densities. We emphasise that in the analysis of the MC the value of  $L_*$  is closely linked to that of  $L_i$ . In Eq. 1 the second and third terms have the same sign, therefore by a slight increase of one of them and a corresponding decrease of the other, one can get a similar agreement with experiment. Figure 2 shows not only the values found from the best fit (the higher  $B$ -region being most sensitive to these two parameters) but also the synchronous variation allowed in these values while retaining a good fit, indicated by arrows. In spite of the variations, there are several trends seen in the figure. First, the value of  $L_i$  is always significantly larger than  $L_*$  and somewhat larger in the better quality sample F2. Second, there is a decrease of  $L_i$  with increasing carrier density, although its value is smaller in the Dirac region. Finally, there is a decrease of  $L_*$  when the carrier density is increased above the Dirac region. The dashed curves in Fig. 2 indicate the expected decrease of  $L_i$  and  $\tau_i$  if the scattering rate is proportional to the density of states, which increases linearly with the Fermi energy  $\epsilon_F \propto V_g^{1/2}$ .

### Estimations of the effects suppressing WL in a single valley

#### *Trigonal warping*

According to [8] the breaking of the time-reversal symmetry in one valley can occur due to the suppression of backscattering by the trigonal warping of the Fermi surface. The trigonal warping rate is

$$\tau_w^{-1} = 2\tau_p(\mu\epsilon_F^2/\hbar v_F^2)^2,$$

where  $\tau_p$  is the momentum relaxation time,  $v_F \approx 10^6$  ms<sup>-1</sup> is the Fermi velocity and  $\mu$  is the

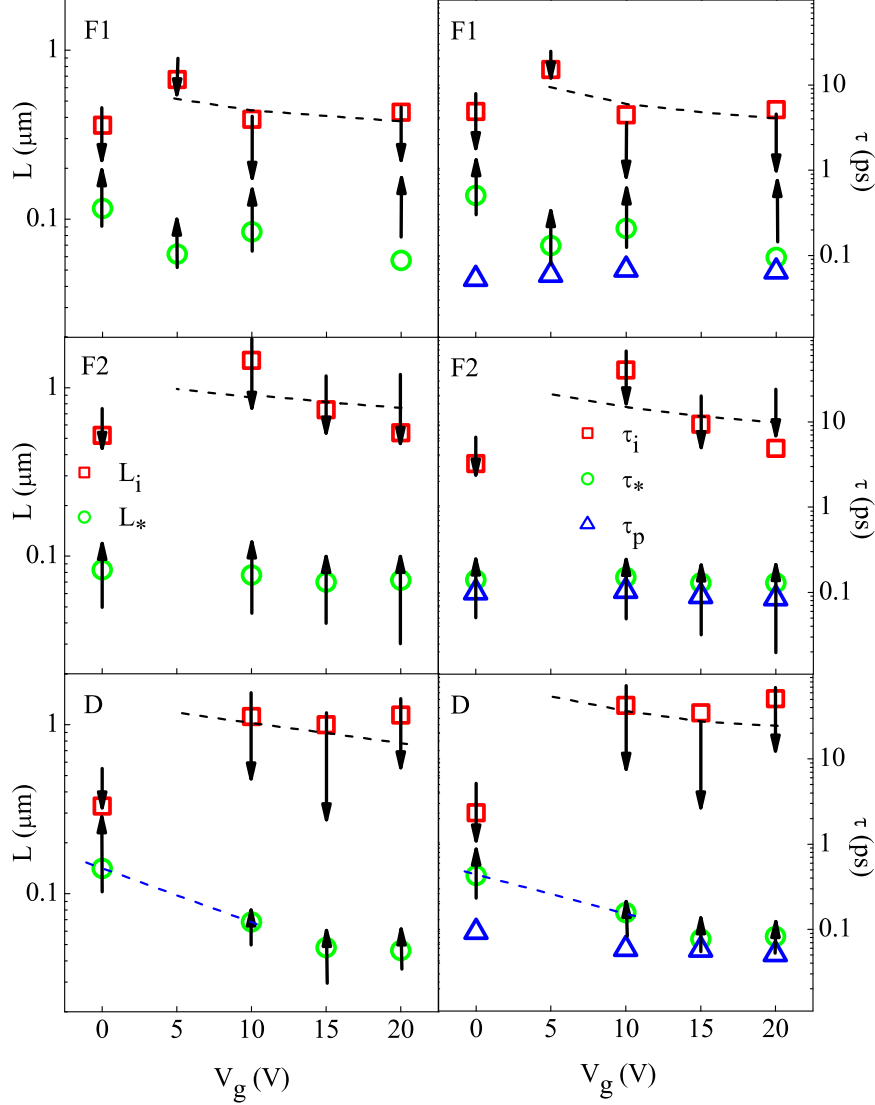


FIG. 2: Comparison of characteristic lengths and times for samples F1, F2 and D at different carrier densities.

structural parameter equal to  $\mu = \gamma_0 a^2 / 8\hbar^2$ . Here  $\gamma_0 \approx 3 \text{ eV}$  is the nearest-neighbour hopping energy and  $a \approx 0.26 \text{ nm}$  is the lattice constant in graphene. For the typical parameters in our samples we obtain  $\tau_w^{-1} \approx 0.001 \text{ ps}^{-1}$  for the Dirac region ( $\epsilon_F \approx 30 \text{ meV}$ ,  $\tau_p \approx 0.1 \text{ ps}$ ) and  $\tau_w^{-1} \approx 0.3 \text{ ps}^{-1}$  for the highest measured concentration ( $\epsilon_F \approx 130 \text{ meV}$ ,  $\tau_p \approx 0.05 \text{ ps}$ ). Trigonal warping of the Fermi surface is therefore a very weak effect compared to other intra-valley scattering mechanisms and cannot be the main reason of the strong chirality-breaking observed in our experiments ( $\tau_*^{-1} \approx \tau_p^{-1}$ ).

### Dislocations

Another possible mechanism of chirality breaking in the graphene sheet is dislocations in the honeycomb lattice [10]. If the trajectory of a quasiparticle goes near the core of a dislocation it leads to a change of the phase due to the induced strain. For randomly distributed dislocations the scattering rate related to this mechanism is

$$\tau_{\text{gauge}}^{-1} \approx \frac{v_F}{k_F \xi^2} ,$$

where  $\xi$  is the average distance between dislocations [10]. In order to obtain the experimentally found chirality-breaking rate  $\tau_*^{-1} \approx 10 - 20 \text{ ps}^{-1}$  the distance  $\xi$  should be about  $15 - 50 \text{ nm}$ . However, the cores of the dislocations should also cause inter-valley scattering, which is why this estimation is in contradiction with the relatively large value of the inter-valley scattering length ( $L_i \approx 1 \mu\text{m}$ ) observed experimentally.

### *Ripples*

As proposed in [5], ripples in the graphene layer on a silica substrate can lead to suppression of weak localization because of the effective magnetic field generated by strain of the interatomic bonds. The vector potential corresponding to a single ripple with diameter  $d$  and height  $h$  is [5]:

$$A = \frac{\gamma_0 |\nabla h|^2}{ev_F} ,$$

where  $\nabla h \approx h/d$ . The flux through one ripple is  $\Phi = \oint \mathbf{A} \cdot d\mathbf{l} \approx Ad$  and  $\Phi = \int \mathbf{B} \cdot d\mathbf{S} \approx Bd^2$ , therefore the magnetic field associated with one ripple is

$$B \approx \frac{A}{d} = \frac{\gamma_0}{ev_F} \frac{h^2}{d^3} .$$

Since the curvature vector of a ripple is random, the resulting magnetic field through the area limited by the dephasing length  $L_\phi$  and containing  $N \approx L_\phi^2/d^2$  ripples should be averaged as follows:

$$B_{\text{eff}} = \frac{B}{\sqrt{N}} = \frac{\gamma_0}{ev_F L_\phi} \left( \frac{h}{d} \right)^2 .$$

The roughness of the graphene sheet found from AFM measurements is about  $0.3 \text{ nm}$  and the size of the features is about  $10 \text{ nm}$ . This gives a value for the magnetic field associated with one ripple  $B \sim 0.1 \text{ T}$ . For our typical value of  $L_\phi \sim 1 \mu\text{m}$  the effective magnetic field is then  $B_{\text{eff}} \sim 1 \text{ mT}$ . Since suppression of the quantum interference requires a magnetic field  $B_{\text{eff}} > B_{\text{tr}} \sim 0.1 \text{ T}$ , the estimated value is too small to destroy the localization effect. The

random magnetic field can only introduce an uncertainty in the value of  $B$ , Fig. 2 of the main text, comparable to the accuracy to which the field is set by the power supply.

### *Potential gradients*

The last mechanism which can produce the breaking of time-reversal symmetry is a gradient of potential coming from the charged impurities in the substrate. A potential gradient leads to a distortion of the dispersion curve of a single valley and hence breaks the valley symmetry. As shown in [10] the resulting scattering rate can be estimated as

$$\tau_{\text{grad}}^{-1} \approx \tau_p^{-1} (k_F a)^2 .$$

In order to get  $\tau_{\text{grad}}^{-1} \approx \tau_p^{-1}$  one should have  $k_F a \approx 1$ . This corresponds to the carrier density  $n = k_F^2/\pi \approx 5 \cdot 10^{14} \text{ cm}^{-2}$ , which is two orders of magnitude higher than the densities studied in the experiment.

We conclude from these calculations that all existing estimations for the chirality-breaking scattering rates are not sufficient to explain our experimental results.

### **Scanning probe microscopy studies**

The atomic force microscope used in this work was an Ntegra Aura from NT-MDT. We used non-contact tips NSG01 with resonance of 150 Hz at an amplitude of  $\lesssim 40 \text{ nm}$ . To obtain high resolution in the  $xy$ -plane ‘diamond-like carbon’ coated tips with curvature radius 1 – 3 nm were used; tip convolution therefore limited feature resolution to this scale. To remove the influence of the water layer present on the silica substrate all measurements were performed in an atmosphere of dry nitrogen at 3 mbar, giving a tip resonance quality factor  $Q \approx 1000$ . The noise in the  $z$ -scale (height) is of the order 0.02 nm measured on pure graphite and silica with the AFM operating with acoustic and vibrational isolation.

We found that the surfaces of the silica and the graphene after lithographic processing were covered in droplets of PMMA with height  $\approx 2 \text{ nm}$ , similar to the findings of [15]. They reduced the image quality and also made determination of the step edge between graphene and silica difficult. To obtain the scans of clean graphene shown in Fig. 4 of the main text we mechanically cleaned the surfaces. Figure 3(a) shows a phase contrast image of sample F2 where both the PMMA droplets and a cleaned area are seen.

To understand the extent to which the PMMA droplets exist under the flake (due to the lithographic process of depositing location markers prior to the deposition of the graphene



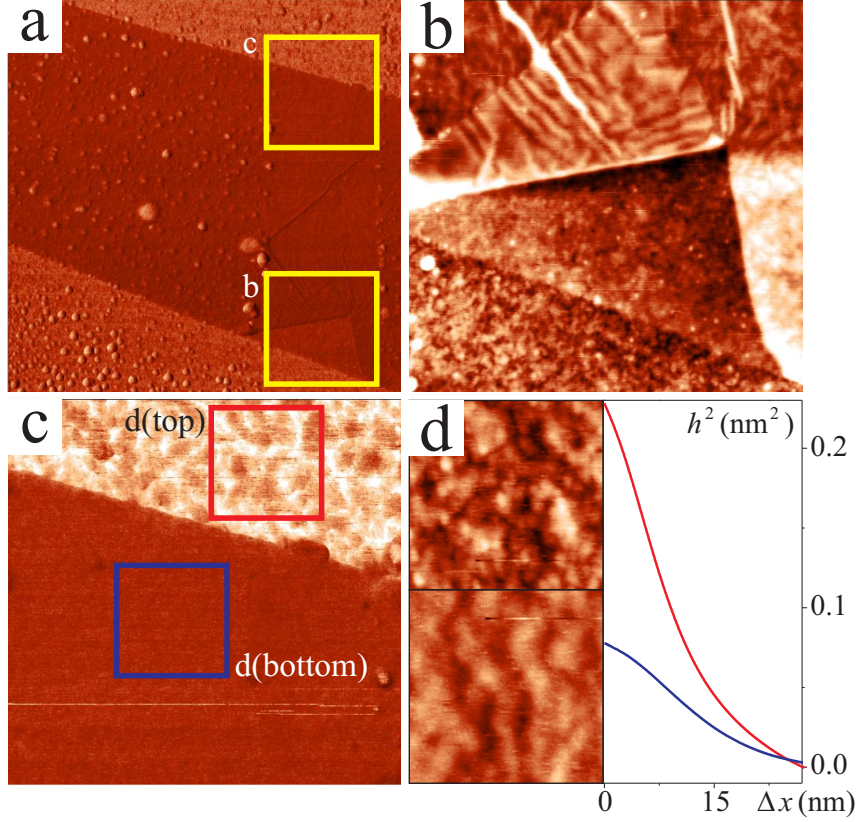


FIG. 3: AFM measurements of sample F2. (a) Phase contrast image where the PMMA droplets on the left and cleaned area on the right can be seen, with two regions in the clean area highlighted by boxes. (b) Magnified topographic image of box ‘(b)’ showing the torn edge of the graphene flake. (c) Magnified phase contrast image of box ‘(c)’ with silica (top) and graphene (bottom). (d) Autocorrelation analysis of the roughness in the boxes highlighted in (c), with insets of silica (top) and graphene topography (bottom). Scan (a) is  $3\mu\text{m}$  size and the phase change at the graphene–silica boundary is  $2^\circ$ . Scans (b)–(c) have the same  $0.8\mu\text{m}$  size. In (b) the colour-scale varies over 4 nm.

flake), we introduced a tear and fold into the sample F2 as seen in Fig. 3(b). We see first that the surface under the flake is indeed free from PMMA droplets and therefore the topography of the flake is only influenced by the silica roughness. (This conclusion was also confirmed by similar measurements on other flakes). Having a flake fold allows us to determine better the thickness of the flake, by measuring the step height between two graphene areas (as opposed to measurements of the step height between silica and graphene which always give a larger value of the step,  $\sim 1\text{ nm}$ ). We find that the thickness of the

flake is  $< 0.5$  nm, which confirms that the flake is a monolayer (supporting the results of the quantum Hall measurements discussed in the main text). An interesting result from the tear is that the graphene flake has a tendency to form larger ripples when detached from the silica surface, with a ripple height  $\sim 0.5$  nm and width 20 nm. (The roughness of the flake on the substrate is  $\sim 0.3$  nm, see the main text.) When comparing the surface roughness of silica and graphene, Fig. 3(c,d), we see that the surface height variation on the clean silica surface is  $\sim 60\%$  larger than on the graphene, i.e. graphene significantly smoothes out the substrate roughness.